

Kinematic Structure of the Orion Nebula Cluster and its Surroundings¹

Gábor Fűrész^{2,3,4}, Lee W. Hartmann⁵, S. Thomas Megeath⁶, Andrew H. Szentgyorgyi²,
Erika T. Hamden⁷

ABSTRACT

We present results from 1351 high resolution spectra of 1215 stars in the Orion Nebula Cluster (ONC) and the surrounding Orion 1c association, obtained with the Hectochelle multiobject echelle spectrograph on the 6.5m MMT. We confirmed 1111 stars as members, based on their radial velocity and/or H α emission. The radial velocity distribution of members shows a dispersion of $\sigma = 3.1 \text{ km s}^{-1}$. We found a substantial north-south velocity gradient and spatially coherent structure in the radial velocity distribution, similar to that seen in the molecular gas in the region. We also identified several binary and high velocity stars, a region exhibiting signs of triggered star formation, and a possible foreground population of stars somewhat older than the ONC. Stars without infrared excesses (as detected with the IRAC instrument on the *Spitzer Space Telescope*) exhibit a wider spread in radial velocity than the infrared excess stars; this spread is mostly due to a blue-shifted population of stars that may constitute a foreground population. We also identify some accreting stars, based on H α , that do not have detectable infrared excesses with IRAC, and thus are potential transitional disk systems (objects with inner disk holes). We propose that the substructure seen both in stellar and gaseous component is the result of non-uniform gravitational collapse to a filamentary distribution of gas. The spatial and kinematic correlation between the stellar and gaseous components suggests the region is very

¹Observations reported here were obtained at the MMT Observatory, a joint facility of the Smithsonian Institution and the University of Arizona

²Center for Astrophysics, 60 Garden Street, Cambridge, MA 02138

³most of this work was done while GF was a research fellow of the Konkoly Observatory of the Hungarian Academy of Sciences, P.O. Box 67, H-1525 Budapest, Hungary

⁴University of Szeged, Department of Experimental Physics, Dom ter 9, H-6723 Szeged, Hungary

⁵Dept. Astronomy, University of Michigan, 500 Church St., 830 Dennison Building, Ann Arbor, MI 48109

⁶Dept. Astronomy, University of Toledo, 2801 West Bancroft Street, Toledo, OH 43606

⁷Dept. Astronomy, Harvard University, Cambridge, MA

young, probably only ~ 1 crossing time old or less to avoid shock dissipation and gravitational interactions which would tend to destroy the correlation between stars and gas.

Subject headings: stars: formation, stars: kinematics, stars: pre-main sequence, clusters: ONC, ISM: kinematics and dynamics

1. Introduction

Because most stars are formed in clusters (e.g., Lada & Lada (2003)), the processes responsible for cluster formation are important to include in any consideration of the mechanisms of star formation. Observations of very young clusters can provide clues to the initial conditions of cluster formation if the cluster has not dynamically relaxed. The increasing sensitivity of infrared studies with both ground-based instruments and the Spitzer Space Telescope has made it more feasible to search for substructure in embedded populations, as seen for example in the young cluster NGC 2264 (Teixeira et al. 2006). In addition, gas and dust can be cleared away rapidly by stellar energy input, revealing many young cluster members at optical wavelengths. In the case of NGC 2264, spatially-coherent kinematic substructure in the stellar population now has been detected using optical spectroscopy by Fűrész et al. (2006).

The Orion Nebula Cluster (ONC) is a touchstone for studies of cluster formation, as it is the closest, relatively populous ($\gtrsim 2000$ members) young cluster containing an O star. While many stars in the ONC are heavily extinguished (Ali & Depoy (1995); McCaughrean & Stauffer (1994); Carpenter, Carpenter et al. (2001); McCaughrean et al. (2002); see also O’dell (2001) and references therein), evaporation of molecular gas by the O6-7 central star θ^1 C Ori has revealed many of the members of the ONC at visible wavelengths. Optical studies of the stellar population show that it is quite young, with a median age of roughly 1 Myr or less (Hillenbrand 1997), suggesting that it is reasonable to search for substructure in the cluster related to the initial conditions of formation.

Hillenbrand & Hartmann (1998, HH98 hereafter) conducted a preliminary study of the structure and kinematics of the ONC. HH98 constructed azimuthally-averaged stellar source counts and showed that they could be fit with a simple, spherically-symmetric, single-mass King cluster model of core radius ~ 0.2 pc and a central density of $\sim 2 \times 10^4$ stars pc^{-3} (see also McCaughrean et al. (2002)). However, HH98 pointed out that the cluster is not circular in projection; rather, it is elongated north-south along the same direction as the molecular gas filament, suggesting that the cluster might not be completely relaxed.

This elongation is particularly apparent on scales larger than 0.5 pc from the center. The filamentary structure is well expressed in CO observations of the region (Bally et al. 1987), as well as in the distribution of pre-main sequence (PMS) stars, shown by recent infrared (IR) observations (Megeath et al 2007, in preparation). According to the models of Burkert & Hartmann (2004), self-gravitationally collapsing gaseous sheets can form such elongated, filament-like clouds. The numerical simulations show that density and velocity dispersion becomes larger at the ends, inducing star formation to start at the tip of the filament, just like the position of ONC within the Orion A cloud. The collapsing sheet model also predicts an overall velocity gradient along the filament, in agreement with CO observations of ONC (Bally et al. 1987). For such a young star forming region as ONC, the stars are still very close to their birthplace; therefore, the stellar kinematics may reflect initial conditions rather than being relaxed.

We therefore conducted a radial velocity (RV) survey of more than 1200 stars in the northern region of the Orion A cloud to search for clues to the initial conditions of the ONC’s formation. In this paper we present results based on high-resolution spectroscopic observations in the $\lambda \sim 6560 \text{ \AA}$ region, which allowed us to measure RVs and identify T Tauri stars (TTS) based on their $H\alpha$ emission. We find that the stellar population exhibits a strong spatial and kinematic correlation with the ^{13}CO gas in the region; the observed substructure conclusively demonstrates that the ONC is not relaxed, but instead reflects the initial conditions involved in its formation. We also comment on the detailed structure, distributional differences seen among stellar groups distinguished by infrared, $H\alpha$, and spatial and kinematic properties. In a subsequent paper we will incorporate followup spectroscopy we have obtained in the Mg triplet region (centered at 5225 \AA) to examine rotational velocities and spectral typing, along with observations of the 6708 \AA Li line to use as an age estimator.

2. Target Selection

To conduct the kinematic study we selected targets in the northern end of Orion A. Thanks to the dense molecular cloud there are few background stars in any stellar catalog of the region. At the same time, the ONC region exhibits a high density of pre-main sequence objects on the sky so the foreground contamination is relatively low. Therefore we initially used a simple color-magnitude selection from the 2MASS catalog to draw the first target list for our observations.

Our intent was to observe multiple fields to cover at least a $\sim 1 \times 2$ degree area. Previous experience with Hectochelle suggested we could reach a S/N ratio of 10 or higher for most

of our targets in 1 hour exposure time if stars with $11.5 < J < 13.5$. We also initially selected stars with $0.2 < (H - K) < 0.5$ to avoid heavily-reddened objects, but this also eliminated many stars with disks (see following paragraph). These selection criteria above therefore resulted in 2319 targets within a 1.5×2.7 degree field centered at $\alpha = 5^h 35^m$ and $\delta = -5^\circ 44'$. This region includes the Trapezium and areas to the south (NGC 1980) and to the north (NGC 1973–1975–1977, NGC 1981) of the ONC.

We added young stellar objects to the sample based on their IR excess as identified using the IRAC and MIPS instruments on board the *Spitzer Space Telescope* (Megeath et al. 2007). This selection went down to a fainter magnitude limit of $J = 15$, and included additional Class II members of the star forming region. These targets were observed during the second of the two spectroscopic runs, while 2MASS selected objects were observed in the first. See Figure 1 for the spatial distribution of selected targets. Details will be given in a forthcoming paper (Megeath et al. 2007).

3. Spectroscopic Observations

The spectroscopic observations were carried out using the Hectochelle multi-object spectrograph (Szentgyorgyi et al. 1998) at the 6.5m MMT telescope in Arizona. We used the 190 Å wide echelle order centered at $H\alpha$, because we could get RV information as well as record the stellar hydrogen emission profiles, a sign of youth and membership, at the same time. This is the same instrumental setup that was used for the observations reported in Fűrész et al. (2006) (see section 2.2 of that paper for details; also Sicilia-Aguilar et al. (2005)).

The first set of spectra was taken in 2004 December, when a total of 866 stars in 4 fields were observed (see Table 1). Initially we chose not to bin in the resolution direction, which resulted in low signal-to-noise (S/N) values for the faintest targets. Therefore, we used a 2×2 binning in 2005 November in order to decrease the readout noise in the data and thus go fainter. Because Hectochelle oversamples the resolution element (the PSF of a resolved spectral feature has ~ 3.5 pixel FWHM), this binning does not result in a serious loss or resolution. Accordingly, the accuracy of RVs derived for the 485 stars observed in 2005 are comparable to the 2004 values.

During the two observing run we collected a total of 1351 spectra of 1215 stars within 7 Hectochelle fields. The location of these objects are shown in Fig 1, overplotted a color IRAC mosaic image covering most of the 1×2.5 degree region explored by spectroscopy.

Sky subtraction would have been very difficult in the vicinity of ONC, as the nebular

emission is so strong and can vary rapidly on small spatial scales. Consequently, placing a few sky sampling fibers over a field is not adequate. The best approach would be to take an offset sky exposure, where all the fibers remain at the target locations and the telescope is moved by a few arcseconds to set targets off the fibers, resulting in sampling the background right next to each targets. However, this procedure would double the exposure time; due to time constraints we did not take such exposures. We simply excluded the emission features not to be important for RV measurements, which did not result in an appreciable loss of absorption features used in the cross-correlations.

4. Data Reduction

The spectra were extracted, calibrated and normalized by an automated, IRAF based pipeline, utilizing the standard spectral reduction packages and tools. Some of the H α emission was so strong that a given aperture became partially saturated, and this affected the H α profile of neighboring apertures. As the RV determination is based on absorption lines outside of the H α region, it usually did not cause problem in measuring RV as we excluded any emission portion of the spectrum from the cross correlation. Sky subtraction was not performed due to the lack of proper background sampling, as mentioned above, so the stellar H α and profiles contain nebular emission (N[II]) is basically all nebular).

The velocities were derived by cross-correlating (CC) each observed spectrum with a set of templates, using the *rvsao* package within the IRAF environment. As we found in Fűrész et al. (2006) by finding the most similar template to a given object in such “multi template method” yields a more accurate RV. Instead of using observed templates, for this present work we adopted synthetic spectra from the library of Munari et al. (2005). Even though the unbinned observations of 2004 yield higher resolution ($R \sim 38,000$) than the $R = 30,000$ for the synthetic ones, downgrading the resolution of the data for the CC was found unnecessary. Comparisons between the cross-correlation functions (CCF) of the original and smoothed (resolution downgraded to match $R \approx 30,000$) data against the same templates showed no differences in the measured RV value larger than the estimated error in fitting the peak of the CCF. For the spectra recorded in 2005 there was an even better match between the resolutions of the data and the templates, due to the 2×2 binning.

The set of templates was a 3 dimensional grid in effective temperature ($3500 < T_{eff} <$

¹IRAF (Image Reduction and Analysis Facility) is distributed by the National Optical Astronomy Observatories, which are operated by the Association of Universities for Research in Astronomy, Inc., under contract with the National Science Foundation.

6000, with 250K steps), surface gravity ($1.0 < \log(g) < 5.0$, with steps of 0.5) and rotational velocity (0,2,5,10,15,20,30,40,50,75 and 100 km s⁻¹). The metallicity was chosen to be $[M/H] = +0.5$, as a possible one for young stars in the solar neighborhood, and its value was fixed because of the common origin of our targets. (Other variables of the full original library were set to: micro-turbulence $K = 2$ km s⁻¹; no $[\alpha/Fe]$ enhancement and using the new ODF models). A total of 1089 templates were compared to each spectrum, and the following values were determined: S , the height of the CCF; R , the signal-to-noise of the CC (for details see Fűrész et al. (2006), Kurtz & Mink (1998) and Tonry & Davis (1979)); V_{rad} , the heliocentric-corrected radial velocity; V_{err} , the error of radial velocity determination. These values are given in Table 2 and 3 along with other result of spectroscopy and photometry.

For each observed spectrum the CCF values of S , R and V_{rad} were plotted and the global peak was localized for S . The parameters of this best fitting template were adopted as the astrophysical parameters of the given star, but only in case if S , R and V_{rad} were changing smoothly within a small range with varying template parameters (as expected for a robust result). We found the variation of these CCF parameters (S , R and V_{rad}) to be a good indicator of noise, as low S/N ratio and/or featureless spectrum yield very different CCFs for different templates, and exhibit no global (outstanding) CCF peak but several local peaks of the same height (0.1-0.2). Significant CCFs yield global peaks at least 30-50% higher than any other noise peak.

We plotted the CCF for the best matching template for each star, and examined the result by eye to make sure the global peak identified did not exhibit any sign of binarity (side-lobes or a secondary peak with comparable peak height). If a companion was found (or a high probability of a possible companion was suggested by the CCF), we marked the star as a binary (possible binary; see Table 2 and 3).

As a result there were 1049 stars out of 1215 yielding an $R > 4$ (only these were used in the later analysis), with a mean R value of 13.7. As a comparison, using 10 actually observed templates (the ones from Fűrész et al. (2006)) we only obtained 547 stars with $R > 4$ and a mean R value of only 7.8. Thus, increasing the number of templates led to a significant increase in the number of objects with accurate RV values.

We found a 0.8 km s⁻¹ offset between the mean heliocentric velocities of the 2004 and 2005 observations. This is likely due to the different (improved) calibration system used in 2005. The shift was determined by comparing velocities of 35 stars observed in both runs with R values larger than 8. The values are listed in Table 2 and 3 are corrected for this zero point offset, by shifting the 2004 values to the 2005 scale.

As discussed by Tonry & Davis (1979), the RV error (ΔV_{rad} in Table 2) is expected to

vary as

$$\Delta V_{rad} \sim W/(1 + R), \quad (1)$$

with W being a constant related to the velocity width of the CCF. We estimated that $W \sim 10 \text{ km s}^{-1}$ and found this to be in good agreement with multiple observations of program objects after correcting for the above zero point offset and eliminating possible binaries.

5. Results

5.1. Velocity Distribution and Correlations Between Stellar and Gaseous Component

The distribution of measured heliocentric radial velocities is shown in Fig. 2. The histogram of the entire sample is displayed for three different S/N ratio of the cross correlation, and we also show the distribution of a spatially selected sub-sample. The $R > 2$ group includes the faintest spectra, on which scattered moonlight causes the the cross-correlation to fix on the solar spectrum rather than the stellar lines; this leads to a false peak near the heliocentric correction value ($\sim 14 \text{ km s}^{-1}$). However, most of the faint spectra follow the distribution drawn by the higher S/N ratio selections. In any event, we did not use any spectra with R values less than 4 in the following analysis.

The distribution of the entire $R > 4$ sample peaks at a heliocentric velocity of 26.1 km s^{-1} (see Gaussian fit on Fig. 2, in good agreement with our initial study of ONC (Sicilia-Aguilar et al. 2005)). The dispersion we found, $\sigma = 3.1 \text{ km s}^{-1}$ (with 10 and 40 km s^{-1} cutoff values), is somewhat higher than the 2.3 km s^{-1} value of the previous Hectochelle study, or the 2.5 km s^{-1} derived from proper motions (Jones & Walker 1988), but the present sample includes a larger region (see Fig. 1). Nevertheless, spatially selecting a sub-sample in the close vicinity of ONC, within a $15'$ radius of Trapezium (292 stars with $R > 4$), we still found a mean velocity of 25.6 km s^{-1} and a dispersion of $\sigma = 3.1 \text{ km s}^{-1}$. These numbers are very close to values calculated using the entire sample, but the distribution is different for these two spatial selections, as it is obvious in Fig. 2. While all the observed stars can be fitted by a $\sigma = 3.1 \text{ km s}^{-1}$ Gaussian, the velocity distribution of ONC stars does not seem sufficiently peaked at the mean velocity.

We computed the cross-correlation between -500 to $+500 \text{ km s}^{-1}$ heliocentric velocities, but found only a small number of stars farther from the peak than $\pm 4 \sigma$. Between $4 - 15 \sigma$ there are stars with high R values, but outside of this region there are only a few, usually very faint, outliers. The insert in the upper left of Fig. 2 shows how clean the distribution

is over the explored RV range, even including the $R > 2$ spectra. The y axis is log scaled, to better show the wings of the peak. (A horizontal line is also drawn at $N = 1$.) Based on the morphology of the histogram we define RV membership for stars with velocities in the $26.1 \pm 4\sigma$ range, or between 13.7 and 38.5 km s⁻¹. Even if the RV was out of this range, or was very uncertain due to low R value, we still considered a star as member if its spectra exhibited non-nebular (i.e., large velocity width) H α emission. For the details on members and non-members see Tables 2 and 3.

Figure 3, 4 and 5 display channel maps, slicing the right ascension–declination–velocity data cube in RV, RA and DEC, respectively. The stars (filled circles) are shown together with the molecular gas (blue shading) in order to compare structure between the stellar and gaseous component. The ¹³CO measurements of Bally et al. (1987) were converted from LSR to heliocentric, to match our RV measurements, by adding 17.5 km s⁻¹ to the LSR values. The size of stellar symbols are coded with R value, larger circle meaning higher S/N in the cross correlation and hence more accurate RV measurements in general. As some stars were observed more than once, we distinguish these by black color as their averaged RV values are even more accurate. All of these maps show an overall north–south gradient in RV and significant substructure.

The morphology seen in the stellar population is very similar to that of the molecular gas. This is most apparent on Fig. 4, where the projection is in RA, as the orientation of the molecular gas has a filamentary structure mostly extending along DEC. To emphasize this structural parallelism, on the last panel of this figure we present a full projection of the ¹³CO data with contour plots of stellar density. (For the contours the number of stars was calculated in 1 km s⁻¹ by 0.1° bins with a grid resolution of 0.5 km s⁻¹ and 0.05°.)

5.2. H α Emission profiles

As described earlier (section 3), we did not take the observations that would be necessary for adequate sky subtraction in this region, where the nebular background can vary strongly over small scales. This makes the analysis of H α profiles difficult, but not impossible in cases where the stellar component is much broader than the (relatively narrow) nebular component. However, nebular emission can be so strong that the stellar signature is barely visible as asymmetries in the wings, at very low intensity levels. This means that neither the canonical 10 Å limit in equivalent width nor the 270 km s⁻¹ limit in full-width at 10% peak (White & Basri 2003) method can be applied on the raw spectra to distinguish between accreting T Tauri stars (classical T Tauri stars, CTTS) and non-accreting, weak-emission T Tauri stars (WTTS).

To help identify the broad wings of $H\alpha$, we used a simple algorithm to identify narrow ($\text{FWHM} < 10 \text{ km s}^{-1}$) emission peaks close ($\pm 25 \text{ km s}^{-1}$) to the main ^{13}CO velocity. and fit a gaussian component to this peak. If such local peak was found than it was replaced with a linear segment, connecting the points where the wider stellar profile started to deviate from the narrow gaussian component. While this helped us to visually inspect the line profiles and make a judgment as to the presence of broad emission wings, it is obviously not a robust method of eliminating nebular emission, especially given the complex velocity structure seen in the densest regions.

In cases of strong nebular emission only the low level wings contain usable information for classification. We therefore examined the linear and log scaled plots of each $H\alpha$ profile. A sample of these plots are presented in Fig. 6. The linearly scaled, corrected profile displayed as a bold line, with a linear segment replacing the supposed and eliminated nebular component. The logarithmically scaled version of the uncorrected spectra is shown as a thin line, and other than emphasizing the wings it also makes it the possible to check if the automated identification and subtraction of nebular emission was correct. (The intensity values does not apply to this representation, as it was scaled to fit the linear-scaled range described above.) Black triangles mark the full width at 10%, which was measured together with EW on the corrected profile. Those values are listed in in Table 2.

We found some contradiction between the two spectroscopy-based classification scheme of TTSS. For some stars even though the nebular-corrected EW (and sometimes the uncorrected EW as well) was significantly smaller than 10 \AA , the full-width at 10% reached or exceeded 250 km s^{-1} , broadening strongly indicative of accretion (for example: 0535495-042438 = F11_ap128; 0534257-045655 = F21_ap115; 0536197-051438 = S1_ap175; etc.). With IRAC photometry in hand for several of these stars we were able to confirm the CTTS status. At the same time in other cases we encountered some disagreement between very clear CTTS profiles and IRAC photometry *not* suggesting a disk (see section 5.3 below). In addition, further uncertainties were caused by the artificial subtraction of nebular emission component.

Therefore the final notes (classes) on $H\alpha$ profiles listed in Table 2 and 3 are based on a somewhat more complicated classification scheme than CTTS/WTTS or no-emission. In cases of very strong nebular emission with apparently broad but uncertain wings in $H\alpha$, to note the possible nebular bias in classification of these stars, we distinguish them with an “NS” prefix in the $H\alpha$ note. A full description of our classification scheme is given in the notes for Tables 2 and 3.

In terms of statistics, in our particular sample the total number of CTTS (including C, CD, CW, NSC, see $H\alpha$ note in Table 2) is 581, or 53.6%, The total WTTS count is 439

(including W, WC, WD, W+, W-, NSW), or 40.5%, for a ratio of $CTTS/WTTS = 1.35$. If only the most confidently classified groups are considered, we have 276 CTTS (including only C), and 230 WTTS (including 160 W and 70 W+), which gives a ratio of $CTTS/WTTS = 1.20$. However, we caution that these numbers *cannot* be used to estimate a true ratio of accreting to non-accreting stars in the region, because our sample is biased by the selection of infrared-excess stars, as well as being limited in the sampling of stars in the inner ONC due to crowding. In addition, our non-IRAC selection of stars (F-fields) tended to omit stars with large infrared excess in H-K.

5.3. Spectroscopic vs. Photometric Disc/Accretion Indicators

The IRAC color-color diagram $[3.6] - [4.5]$ vs. $[5.8] - [8.0]$ (Allen et al. 2004) can be used to distinguish between young stars with and without inner disk emission (and protostars with circumstellar envelopes, but these were not within the scope of our survey). In the case of a star having both short- and long wavelength infrared excess due to a circumstellar disk, accretion onto the star is likely taking place, and therefore we expect a broad $H\alpha$ profile, (the signature of material falling in at high velocity), thus a CTTS (e.g., White & Basri 2003). If the short wavelength excess is not present, presumably there is either no disk to accrete or no inner disk; in most cases, such systems are not accreting and thus are WTTS.

Fig. 7 shows that as expected, many weak-emission stars have no infrared excesses and many wide-emission stars have infrared excesses, but there are a significant number of counterexamples. We suspect that many, if not all, of the stars with significant $[3.6]$ - $[4.5]$ excesses are in fact accreting, based on the strong correlation previously seen in K-L in Taurus (Hartigan et al. 1990), but the strong nebular contamination prevents us from detecting the $H\alpha$ wings. Other objects with only long-wavelength excesses may indeed not be accreting. In addition, there are systems without any excesses which clearly are accreting. In the cases of 0533477-045208 (F11_ap43) or 0535343-060542 (F31_ap158) the IRAC colors are $[3.6 - 4.5] = 0.06 / 0.07$, $[5.8 - 8.0] = 0.41 / 0.13$, respectively, both stars have high S/N ratio spectra with very prominent, wide $H\alpha$ emission containing only negligible, easily identified nebular components. In contrast, 0535513-061353 (F31_ap208) and 0536222-055547 (S3_ap217) the IRAC colors show clear excess, $[3.6 - 4.5] = 0.39 / 0.34$, $[5.8 - 8.0] = 0.87 / 0.75$, but the well defined spectrum shows only a weak nebular component with slight asymmetry or very low level wings.

F11_ap43 and F31_ap158 appear to be examples of a small class of objects termed “transitional disks” (Calvet et al. 2002, 2005). We have found ~ 35 such stars in our ONC sample. These systems tend to have their inner disks partially or almost totally cleared of

small dust, as inferred by the weakness of the near-infrared excess, yet have substantial outer disks. TW Hya (Calvet et al. 2002, 2005) and DM Tau (Calvet et al. 2005) are examples of systems which have essentially zero measurable excesses shortward of $\sim 5\mu\text{m}$ but have strong excesses at longer wavelengths, and *in addition* are still accreting gas onto the central star, producing a broad H α emission profile. (For example, the 10-Myr-old accreting T Tauri star TW Hya has IRAC colors of [3.6] - [4.5] = 0, [5.6] - [8] = 0.95; Hartmann et al. 2005.) Megeath (personal communication) has confirmed the transitional disk status of these objects, as his Spitzer photometric survey extended into the 24 μm band and some of these peculiar stars had usable (acceptable S/N ratio) measurements exhibiting long wavelength excess.

How small dust “disappears” while gas still accretes in the inner disk is not entirely clear. One possibility is that grains grow to such large sizes that the near-infrared opacity is reduced; another possibility is that “filtration” occurs at the inner edge of the optically-thick outer disk, moving particles of sizes responsible for the near-infrared emission outward (Rice et al. 2006). In any event, the accreting transition disks we identify here in the ONC must be among the very youngest such systems known, expanding the range of ages where transitional disk behavior occurs.

5.4. Binary Stars

As the velocity dispersion in the ONC region is relatively small, identifying spectroscopic binaries is important to explore intrinsic kinematic structure. To ensure a consistent zero-point (see Section 4) between the multi-epoch observations discussed here, we included some stars of our first observing run in the second set. Also, to make sure that different fields of a given run have a common zero point, we had some overlap between fields so that some stars were observed multiple times within an observing run. Out of the 1215 targeted stars 1086 were observed only once, 122 twice, and 7 three times. For the 129 stars observed multiple times, we compared RV values and evaluated the difference (Δ) against the internal RV error (σ) of the correlation, identifying possible ($\Delta > 1.5\sigma$) and likely ($\Delta > 3\sigma$) binary stars. The *CCF* column of Table 2 and 3 lists *dv?* and *dv* notes for these stars, respectively.

In case of a single RV measurement the cross correlation function still can be used to identify double-lined spectroscopic binary stars. By looking at each individual CCF we found several side lobes, secondary peaks blended with the main peak (CCF note *s*), and resolved double peaks (*d*). In case the main/secondary CCF peak heights were not at least 50% higher than any other local peaks due to noise, or the side lobe did not raise 25% higher than local peaks and therefore the detection probability was not high, we added the “?” sign in the notes to express the uncertainty.

The location of these binary stars are shown in Figure 8, displayed as a full projection in RA, onto a RV–declination plane. The possible (more uncertain) stars are shown with open triangles, the more likely candidates noted with open diamonds. The velocity used for plotting is the average of all measured RV values in case we had more than one measurement. A wider velocity range is applied to this plot to accommodate all the binary stars, rendering the main stream cluster members and molecular gas into a narrow vertical feature. Counting all the possible (18) and more likely ones (34), the total number of binaries is 52, or $\sim 4\%$ of the entire sample.

Based on these single epoch observations we cannot make an estimate of the spectroscopic binary fraction of the ONC. However, our results may be consistent with the low frequency of resolved multiple systems suggested for the ONC (see Köhler (2006) and references therein). In any event, our observation of position-velocity structure in the stellar distribution, which strongly correlates with the molecular gas, indicates that the overall dynamics are not strongly biased by binary motion, though our velocity dispersions may be slightly inflated due to orbital motion. Of course, there may be spectroscopic binaries present in our sample with much smaller velocity shifts that are difficult to separate from the main population (see §6.3).

5.5. High Radial Velocity Stars

In section 5.1 we showed that the RV distribution is relatively clean, with very few outliers from the main peak (see insert of Fig. 2). Although most of these high velocities are just false detections (the CCF peak found to be global is just marginally higher than any other local peak due to noise), some are real (a global CCF peak more than 50% higher than other local peaks); these stars have a note “R” in the $H\alpha$ column of Table 3. What makes these stars interesting is the possibility that they originated from a cluster by a decay of a triple or multiple young stellar system, or by interaction of multiple systems (Gualandris et al. 2004) and then were ejected at high velocities. The very high stellar density of ONC makes it a favorable place to look for such stars (one example may be the BN object, just north-west to the Trapezium (Rodríguez et al. 2005)). Three members of ONC were recently suggested by Poveda et al. (2005) to be possible runaway stars based on proper motion measurements performed on photographic plates, but O’Dell et al. (2005) did not confirm these motions using proper motion measurements from Hubble Space Telescope images. Only one of these three stars (JW 355) can be found in our sample as 0535109-052246 (S2_ap220). Unfortunately the spectrum is very noisy so we have no additional radial velocity measurement.

Among our targets we have 21 stars with the “R” note, out of which 5 stars have velocities smaller than -40 km s^{-1} (more than $\sim 20\sigma$ off the mean cloud velocity) and 15 have RV values larger than 80 km s^{-1} . Each of these stars were observed only once so the only hint for companions, as an other possible reason of deviant RV, would be the CCF. However, for all of them it only has a single, well defined peak.

A relation to the cluster is apparent only in one case, as star 0535503-044208 (F11_ap146) shows $\text{H}\alpha$ emission (therefore listed in Table 2). All the others exhibit only a nebular emission component superimposed on the $\text{H}\alpha$ absorption line. According to the stellar parameters derived from the multi-template fitting, more than half of these stars are K–M dwarfs. Assuming main sequence colors (Kenyon & Hartmann 1995), based on the derived temperature, and comparing it to the observed (J-H) value, we got extinction values of $A_V \simeq 3 - 4$ by assuming a $E(J - H) = 0.19 E(B - V)$ relation (Bessell & Brett 1988). This is a plausible value in those areas these stars are located, farther from dense regions.

The three most deviant RV stars are worth mentioning. One object is blueshifted at $RV = -147 \text{ km s}^{-1}$, and exhibits only $A_V = 1.3$. The low extinction is not surprising as this star (0537111-055946 or F31_ap162) is located at the very edge of our field, which also means just off to the side of the Orion A molecular cloud. The surface gravity suggests a giant, thus it is likely a background object based on its brightness. This is in agreement with its location, as we could have not observed it behind the denser parts of the cloud.

The two highly redshifted stars (0536592-050029 or F11_ap183 at $RV = 232.5 \text{ km s}^{-1}$; and 0537005-050931 or F22_ap138 at $RV = 438.7 \text{ km s}^{-1}$) have almost the same RA value as F31_ap162, so those are also just off the cloud. The former star seems to have a low surface gravity, and therefore it is likely a background object as well, at a brightness of $J = 11.87$. However, there seems to be a contradiction with its J magnitude, as the $(J - H) = 1.09$ color suggests a very high extinction adopting the intrinsic colors of $(J - H)_0 = 0.66$ from Alonso et al. (1999), based on the stellar parameters derived from template fitting. Another problem with the interpretation as a background object is that the $[Fe/H] = +0.5$ templates used for the analysis might be not adequate. Re-running the cross-correlation on a grid of metallicities (with a fixed rotational velocity of 0) it turns out a $[Fe/H] = -0.5$ gives a better match (with $T_{eff} = 4500$ and $\log(g) = 1.5$), but the observed and intrinsic colors are still in contradiction with the expected low extinction. Thus, additional spectroscopy is required to say more about this object.

Exploring metallicity by further template matching turned out to be crucial for the highest radial velocity star, F22_ap138, as for temperature we hit the edge of parameter space while performing cross-correlation of the original grid. Fixing the rotational velocity at 0 and exploring a metallicity–temperature–gravity grid we found the best match to be

a $[Fe/H] = -1.5$ spectrum with $T_{eff} = 4250$ and $\log(g) = 4.0$. This results a plausible extinction of $A_V = 1.1$. The low metallicity template suggests that this is not a young star, therefore very likely we witness a fast moving background member of an older population.

6. Discussion

6.1. Cluster in Formation

The significant position-velocity substructure seen in both the stars and the molecular gas clearly demonstrates that the ONC is not dynamically relaxed; qualitatively, it appears to be more consistent with dynamical models of cluster formation such as those of Hartmann & Burkert (2007) and Bate, Bonnell, & Bromm (2003). The curvature of the ^{13}CO emission seen in the northern region of the position-velocity plot (Figure 4), with a possible corresponding southern feature, is suggestive of gravitational acceleration of material toward the cluster center, where the gravitational potential well should be deepest. Gravitational acceleration is also consistent with the evidence for the largest velocity distribution in the gas located near the center. Many stars exhibit the same position-velocity distribution as the ^{13}CO , which suggests that these stars are mostly following the motion of the dense gas within which they formed. If these motions were primarily the result of stellar energy input through winds or photoionization, it is not clear that the gas and many stars should show the same kinematics, as such energy input could easily blow the gas away from the stars - some possible examples of this are discussed in the following section.

The observed correlation of stars and dense gas in space and in velocity indicates that the inner regions cannot have experienced more than about one crossing or collapse time; otherwise the velocity structure would be erased as the infalling gas shocks and dissipates its kinetic energy, with the stars passing through the shocked gas. Overall, the spatial coherence in the ^{13}CO gas kinematics, the evidence that many younger stars follow this motion, and the strongly filamentary structure of the stellar distribution outside the main core of the ONC suggest that the ONC still exhibits features traceable to its initial conditions of formation.

6.2. Subgroups and stellar energy input

While there is a strong general spatial and kinematic correlation between stars and dense gas, there are exceptions. One especially clear case can be seen on the bottom left panel of Fig. 4 at $DEC \simeq -5^\circ 27'$: a tight, linear string of stars sticking out of the main cloud as a “nose” extending between $RV = 21$ and 25 km s^{-1} . The left-hand panel of 9

shows a declination-velocity plot zoomed into this region, in an RA range shifted slightly westward of the Trapezium region (vertical lines in the right-hand, RA-DEC panel of Fig. 9). Clearly there is a small group of stars blueshifted by about $1\text{--}2 \text{ km s}^{-1}$ from the gas in the declination range $-5^d 20^m > DEC > -5^d 30^m$. Selecting “off-cloud” stars by means of an velocity envelope for the gas (thin curve in left panel) results in demonstrating that these stars are spatially concentrated in a region south-west of the Trapezium which is relatively evacuated, as indicated by the weak $8\mu\text{m}$ emission seen in the IRAC map (right panel, grayscale). This region is also known for a large number of Herbig-Haro objects shaped like bow-shocks pointing back toward the Trapezium region (see description in O’dell (2001)), consistent with the idea that outflows from the region of most current star formation is blowing out material.

We therefore suggest that the molecular gas in this region originally extended to more negative velocities, but that outflows have cleared away the gas, making an “indentation” in the position-velocity plot at $\sim -5^d 26^m$, $RV \sim 24 \text{ km s}^{-1}$, and leaving the recently-formed stars behind.

There are other interesting small scale structures, like the tight, dense sub-cluster group seen in the middle of the second panel of Fig. 5 (upper row, 2nd panel from left to right, also somewhat apparent on Fig. 4 upper row, rightmost panel). These can be remnants of small building blocks, traces of density variations in the primordial cloud.

6.3. Other Populations?

Based on Fig. 7, we divided our sample into *IR-excess sources*, with $([3.6] - [4.5]) > 0.2$ and $([5.8] - [8.0]) > 0.5$; and *non-IR excess sources* with $([3.6] - [4.5]) < 0.2$ and $([5.8] - [8.0]) < 0.5$. This division of sources is shown on the velocity-declination map with full projection along RA in Figure 10: the left panel for excess and the middle one for non-excess stars.

Looking at the left panel in Figure 10, southward of -6° there are very few CTTS. This abrupt change is an unfortunate selection effect. The targets selected for our second observing run (S fields) had a southern declination limit of -6° , exactly where the sudden change of excess/non-excess ratio happens. And since targets for the first observing run (F fields) were selected from the 2MASS color-magnitude diagram, our selection was biased against stars with IR excesses because of the $(H - K) < 0.5$ criterion.

While many of the non-excess stars (middle panel) follow the general distribution of gas and excess stars, a modest number clearly exhibit a broader distribution in radial velocity,

with more blue- than redshifted stars. This can be seen on the right panel, where we present RV histograms of excess (solid bars) and non-excess (gray-shaded boxes) stars, for three declination ranges (north, with $DEC > -5.2$; mid, with $-5.2 > DEC > -6.0$; and south, $DEC < -6.0$ - as represented by the location of the histograms as well). We divided this way because RV behavior of the gas is very different in these regions: the northern velocity is significantly higher than the mean velocity in the south, and the middle section exhibits a strong RV gradient. Regardless, the velocity distribution of non-excess stars is wider because of a secondary peak at lower velocities.

One possibility is that the lower-velocity stars have been ejected from the main cluster. Close encounters in multiple star systems might result in ejecting stars while stripping their disks; the red-shifted stars might then eventually plunge into the dense, opaque regions behind, leaving more optically-visible stars with blueshifts. However, this seems unlikely because it requires a surprisingly large fraction of stars to be ejected, we do not detect a larger density of such objects nearer the center of the ONC, where the high stellar density would be more favorable to ejection. In addition, south of -6° the velocity distribution is clearly bimodal, with a very tight velocity spread for the on-cloud stars; it is not clear why ejection would lead to such distinct structures.

Another possibility is that we are detecting a foreground, older population. Stars in the foreground Orion 1a association (Brown et al. 1994) may have a heliocentric radial velocity near $\sim 20 \text{ km s}^{-1}$, as suggested by measurements of the 25 Ori group Briceño et al. (2007). If this is the case, it would mean that the Orion 1a association is much more spread spatially towards the ONC (in the foreground) than has previously been realized.

A third possibility is that stellar energy input blew out material, forming a small proportion of stars in a bubble wall moving toward us. To explore this idea further, we plot only the stars with RV values less than 22 km s^{-1} in the RA–DEC plot of Figure 11. Since there is no gas here, we display the most blueshifted 1 km s^{-1} wide channel of the gas at 23 km s^{-1} heliocentric velocity. The northern foreground stars seems to be separated from the older southern group, by an almost empty gap running east–west at $-6^\circ 00'$. However, this might be the result of a combination of our bias against selecting infrared-excess stars mentioned above and accidental fiber coverage. Still, there is some structural similarity between the distribution of these southern foreground stars and the gas “behind”, redshifted to it. Note how these southern stars are spread on top of two-three denser gas clumps. If this structure is interpreted as a local “bubble”, this could have been created at the very beginning of star formation by the early emergence of some OB stars in the region. These stars than could have blown away most of the gas from us, some smaller amount towards us, and so other stars could have formed at this early stage in this perturbed southern region.

This picture would require some OB stars in the questioned region, and the list of Brown et al. (1994) contains six of them interestingly close to -6 degree declination (see Fig. 11). However, obviously none of these is in close vicinity of the gas now, as there are no apparent HII regions at this part of the molecular cloud. An additional problem is that one would expect such a population to be somewhat older than the main cloud, which is not obvious in the J vs. J-H diagram. This is not a particular problem for the foreground population hypothesis, as the Orion 1a stars will appear higher in the color-magnitude diagram at a given age than the ONC.

In conclusion, the reasons for the additional velocity spread of the non-excess stars are not clear. Further monitoring for radial velocity variations as well as more detailed studies of the stellar properties are needed to determine which of the above possibilities are correct.

6.4. Comparison with Other Observations and Models

If the ONC is not dynamically relaxed, why did HH98 find a fairly good fit to a King cluster model? (Note that Scally et al. (2005) point out difficulties with physically interpreting the ONC in this way). The central region of radius ~ 0.5 pc does appear to exhibit a smooth distribution, and thus may be closer to having relaxed, though it is somewhat elongated. On larger scales, the elongation is sufficiently large that azimuthal averaging is not appropriate. To take an extreme example of what this averaging can do, imagine a cylindrical distribution of material in the plane of the sky with uniform surface density and width W . Azimuthal averaging of this distribution results in an average surface density $\Sigma \sim \text{constant}$ for $r < W$ and $\Sigma \propto r^{-1}$ for $r \gg W$. Interpreting this surface density in terms of a spherically-symmetric density distribution results in $\rho \sim \text{constant}$ for $r < W$ and $\rho \propto r^{-2}$ for $r \gg W$, which is roughly consistent with a King model. The ONC is not as extreme in structure as this simple example, but it illustrates the potentially misleading nature of azimuthal averaging of an intrinsically highly elongated structure.

Comparing azimuthally averaged stellar densities and global velocity dispersions to N-body calculations, Kroupa (2000) was unable to distinguish whether the ONC is in equilibrium, or is collapsing, or is expanding; a similar result was obtained Scally et al. (2005). This demonstrates the importance of avoiding azimuthal averaging and obtaining detailed kinematic observations of gas and stars in developing an understanding of the dynamical state of the region.

Tan, Krumholz, & McKee (2006; TKM06) have argued for a picture in which rich star clusters take several dynamical times to form, are quasi-equilibrium structures during

formation, and thus initial conditions are not very important. In particular, TKM06 discuss the ONC and argue that it is several crossing times old, of order 3 Myr, larger than assumed here. Here we discuss why we arrive at different conclusions.

Following Scally & Clarke (2002), TKM06 argue that the smoothness of the spatial distribution of the stars in the ONC argues for long formation times, which allow clumps of stars to disperse. As pointed out above, the azimuthal averaging done by Hillenbrand & Hartmann (1998) was somewhat misleading, helping to smooth out filamentary structure. In addition, the gas kinematics, and to a lesser extent the stellar kinematics, show substructure which is less evident in the spatial distribution alone.

TKM06 also use the analysis of stellar ages in the $0.4\text{--}6M_{\odot}$ mass range by Palla & Stahler (1999) to argue for a large age spread in the ONC. Although they note that Hartmann (2003) pointed out problems of contamination by non-members, TKM06 do not take sufficient notice of the mass-dependence of isochrones. As was clear from the original work by Hillenbrand (1997), and is evident in Figure 4 of Palla & Stahler (2000), standard isochrones imply that stars of 1 to $5 M_{\odot}$ in the ONC have systematically older ages by one to a few Myr than both the lower mass stars and the higher mass stars. This effect is seen in virtually every star-forming region, at least comparing the intermediate mass stars to the lower mass $< 1M_{\odot}$ stars (see HR diagrams in Palla & Stahler (2000)). In other words, the “tail” of older stars in the distribution of stellar ages found by Palla & Stahler (1999, 2000) is strongly populated by a *different* mass range (intermediate mass stars) than the peak of the age distribution (low mass stars).

As pointed out by Hartmann (2003), if one takes these age determinations at face value, it means that the ONC existed for a few Myr as a cluster forming mostly intermediate mass stars, with very few low mass stars (or high-mass stars). In other words, the ONC (and other regions) begin their first few Myr of existence with extremely non-standard stellar initial mass functions (IMFs). There is no observational evidence for any young clusters dominated by intermediate-mass stars by number. Therefore, there must be something wrong with the isochrones.

Pre-main sequence ages are contraction ages; one must know the starting radius of the star to determine the age. TKM06 argue that corrections for starting radii (the “birthline” position) are only important for stars with ages < 1 Myr. However, Hartmann (2003) showed that this is not necessarily true for intermediate-mass stars; changing the accretion rates at which stars form over plausible ranges can have very big effects on the birthline for $\gtrsim 1M_{\odot}$ stars. Thus, the apparent ages of the intermediate-mass stars can be systematically overestimated due to incorrect birthline assumptions; this allows the ONC to maintain a roughly typical IMF over its formation. With this correction, the fraction of stars older than

2 Myr decreases dramatically.

7. Summary

We have carried out a spectroscopic survey of 1215 stars located in the northern end of Orion A molecular cloud, covering the ONC and its vicinity. The obtained radial velocities show a well defined spatial and kinematical structure of the stellar component, which is very similar to the one seen in the molecular gas. Comparing our observational results to the model of Hartmann & Burkert (2007), we draw the following picture of the ONC region:

On large scales the gas (and stars) exhibit a velocity gradient due to rotation or shear running north-south. The curvature seen most clearly in the northern arm of the gas in the position-velocity diagrams suggests gravitational acceleration towards the cluster center. We further conjecture that the concentration of gas (and stars) south of the Trapezium region is somewhat in front and is also falling in towards the center, explaining its higher radial velocities; the Orion Bar photodissociation region appears to reside just above, or perhaps at the upper edge, of this moving clump. The southern part of the filament may also be falling in, although the motions are much less organized than is apparent in the northern arm. Finally, it may be possible that the process of blowing out the near side of the cloud, in the south, resulted in accelerating and compressing gas which formed a small population of stars with velocities blueshifted by a few km s^{-1} ; or, these stars may be foreground objects in a different kinematic system possibly associated with Orion OB 1a.

The high degree agreement between the structure of the gaseous and stellar component suggest the region is very young, only ~ 1 crossing time old, otherwise gravitational interaction should have been smoothed the fine structure still clearly visible in our data. Note that the observational errors for the stellar radial velocities (ranging from 0.5 - 1.5 kms) are larger than the observational errors in the radio measurements. In addition, with only two epochs (at most) we cannot correct for the effects of even small binary motion. For these reasons it is not yet possible to make fine distinctions between stellar and gas kinematics.

The spectra in the $\text{H}\alpha$ order provide not only RV measurements but allow the possibility of classifying many stars according to their $\text{H}\alpha$ emission. With the aid of IRAC photometry we were able to confirm the presence of disk around many CTTS opening/loss of a disk around most WTTS. To the south we see another older but foreground population, which still might be not completely independent but connected to the region, suggested by continuous streams of stars to the south and north of this group and by the similarity in the spatial structure of the “background” gas and these blueshifted stars.

In a future communication we will provide further improvements in the detection of spectroscopic binaries and provide additional checks on membership using the 6708 Å Li line.

We would like to thank for the MMT observers and instrument support team for all their efforts to make Hectochelle work and for providing continuous help in the preparation of the observations and in data acquisition: Perry Berlind, Mike Calkins, Maureen Conroy, Dan Fabricant and John Roll. Lori Allen's comments were very useful in making the text comprehensive. This work was supported in part by NASA grant NNG06GJ32G.

REFERENCES

- Ali, B., & Depoy, D. L. 1995, *AJ*, 109, 709
- Allen, L.E. et al., 2004, *ApJS*, 154, 363
- Alonso, A., Arribas, S., & Martínez-Roger, C. 1999, *A&AS*, 140, 261
- Appenzeller, I., Bertout, C., & Stahl, O. 2005, *a*, 434, 1005
- Bally, J., Stark, A.A., Wilson, R.W., & Langer, W.D. 1987, *ApJ*, 312, 45
- Bate, M. R., Bonnell, I. A., & Bromm, V. 2003, *MNRAS*, 339, 577
- Bessell, M.S., & Brett, J.M. 1988, *PASP*, 100, 1134
- Bonnell, I.A., & Bate, M.R. 2006, *MNRAS*, 370, 488
- Briceño, C, Hartmann, L., Hernandez, J., Calvet, N.; Katherina Vivas, A., Furesz G., & Szentgyorgyi, A. 2007, *ApJ*, 661, 1119
- Broos, P.S., Feigelson, E.D., Townsley, L.K., Getman, K.V., Wang, J., Garmire, G.P., Jiang, Z., & Tsuboi, Y. 2007, *ApJS*, 169, 353
- Brown, A.G.A., de Geus, E.J., & de Zeeuw, P.T. 1994, *A&A*, 289, 101
- Burkert, A., & Hartmann, L. 2004, *ApJ*, 616, 288
- Calvet, N., D'Alessio, P., Hartmann, L., Wilner, D., Walsh, A., & Sitko, M. 2002, *ApJ*, 568, 1008
- Calvet, N., et al. 2005, *ApJ*, 630, L185

- Carpenter, J.M., Hillenbrand, L.A., & Skrutskie, M.F. 2001, *AJ*, 121, 3160
- Fűrész, G., Hartmann, L.W., Szentgyorgyi, A.H., Ridge, N.A., Rebull, L., Stauffer, J., Latham, D.W., Conroy, M.A., Fabricant, D.G., & Roll, J. 2006, *ApJ*, 648, 1090
- Gualandris, A., Portegies Zwart, S., & Eggleton, P.P. 2004, *MNRAS*, 350, 615
- Gutermuth, R.A. 2005, PhD Thesis, University of Rochester, NY
- Hartigan, P., Hartmann, L., Kenyon, S. J., Strom, S. E., & Skrutskie, M. F. 1990, *ApJ*, 354, L25
- Hartmann, L. 2003, *ApJ*, 585, 398
- Hartmann, L., Megeath, S. T., Allen, L., Luhman, K., Calvet, N., D'Alessio, P., Franco-Hernandez, R., & Fazio, G. 2005, *ApJ*, 629, 881
- Hartmann, L., & Burkert, A. 2007, *ApJ*, 654, 988
- Hernández, J., Calvet, N., Hartmann, L., Briceño, C., Sicilia-Aguilar, A., & Berlind, P. 2005, *AJ*, 129, 856
- Hernández, J., et al. 2007, *ApJ*, 662, 1067
- Hillenbrand, L.A 1997, *AJ*, 113, 1733
- Hillenbrand, L.A, & Hartmann, L.W. 1998, *ApJ*, 492, 540
- Jensen, E. L. N., & Mathieu, R. D. 1997, *AJ*, 114, 301
- Jones, B.F., & Walker, M.F. 1988, *AJ*, 95, 1755
- Kenyon, S.J., & Hartmann, L. 1993, *ApJS*, 101, 117
- Köhler, R., Petr-Gotzens, M.G., McCaughrean, M.J., Bouvier, J., Duchene, G., Quirrenbach, A., & Zinnecker, H. 2006, *A&A*, 458, 461
- Kroupa, P. 2000, *New Astronomy*, 4, 615
- Kurosawa, R., Harries, T.J., & Symington, N.H. 2006, *MNRAS*, 370, 580
- Kurucz, R. 1979, *ApJS*, 40, 1
- Kurtz, M.J., & Mink, D.J. 1998, *PASP*, 110, 934
- Lada, C. J., & Lada, E. A. 2003, *ARA&A*, 41, 57

- Marchenko et al. 2000, MNRAS, 317, 333
- McCaughrean, M.J., & Stauffer, J. R. 1994, AJ, 108, 1382
- McCaughrean, M.J., Zinnecker, H., Andersen, M., Meeus, G., & Lodieu N. 2002, ESO Messenger, 109, 28
- Megeath, S.T. et al. , in preparation
- Munari, U., Sordo, R., Castelli, F., & Zwitter, T. 2005, *Å*, 442, 1127
- O'dell, C.R. 2001, ARA&A, 39, 99
- O'Dell, C.R., Poveda, A., Allen, C., & Robberto, M. 2005, ApJ, 633, 450
- Palla, F., & Stahler, S.W. 1999, ApJ, 525, 772
- Palla, F., & Stahler, S.W. 2000, ApJ, 540, 255
- Poveda, A., Allen, C., & Hernandez-Alcántara, A. 2005, ApJ, 627, 61
- Rice, W. K. M., Armitage, P. J., Wood, K., & Lodato, G. 2006, MNRAS, 373, 1619
- Reipurth, B., Pedrosa, A., & Lago, M.T.V.T. 1996, A&A Suppl., 120, 229
- Rodríguez, L.F., Poveda, A., Lizano, S., & Allen, C. 2005, ApJ, 627, 65
- Scally, A., & Clarke, C. 2002, MNRAS, 334, 156
- Scally, A., Clarke, C., & McCaughrean, M.J. 2005, MNRAS, 358, 742
- Sicilia-Aguilar, S., Hartmann, L.W., Szentgyorgyi, A.H., Fabricant, D.G., Fűrész, G., Roll, J.B., Conroy, M.A., Calvet, N., Tokarz, S., & Hernández, J. 2005, AJ, 129, 363
- Stahler, S.W., & Walter, F.M. 1993, in Protostars and Planets III, ed. E.H. Levy & J.I. Lunin (Tucson: University of Arizona), 405
- Stickland, D.J., Pike, C.D., Lloyd, C., & Howarth, I.D. 1987, A&A, 184, 185
- Szentgyorgyi, A.H., Cheimets, P., Eng, R., Fabricant, D.G., Geary, J.C., Hartmann, L., Pieri, M.R., & Roll, J.B. 1998, Proc. SPIE, 3355, 242
- Tan, J.C., Krumholz, M.R., & McKee, C.F. 2006, ApJ, 641, L121 (TKM06)
- Teixeira, P. S., et al. 2006, ApJ, 636, L45

Tonry, J. & Davis, M. 1979, AJ, 84, 1511

Wang, J., Townsley, L.K., Feigelson, E.D.; Getman, K.V., Broos, P.S., Garmire, G.P., & Tsujimoto, M. 2007, ApJS, 168, 100

White, R.J., & Basri, G. 2003, AJ, 582, 1109

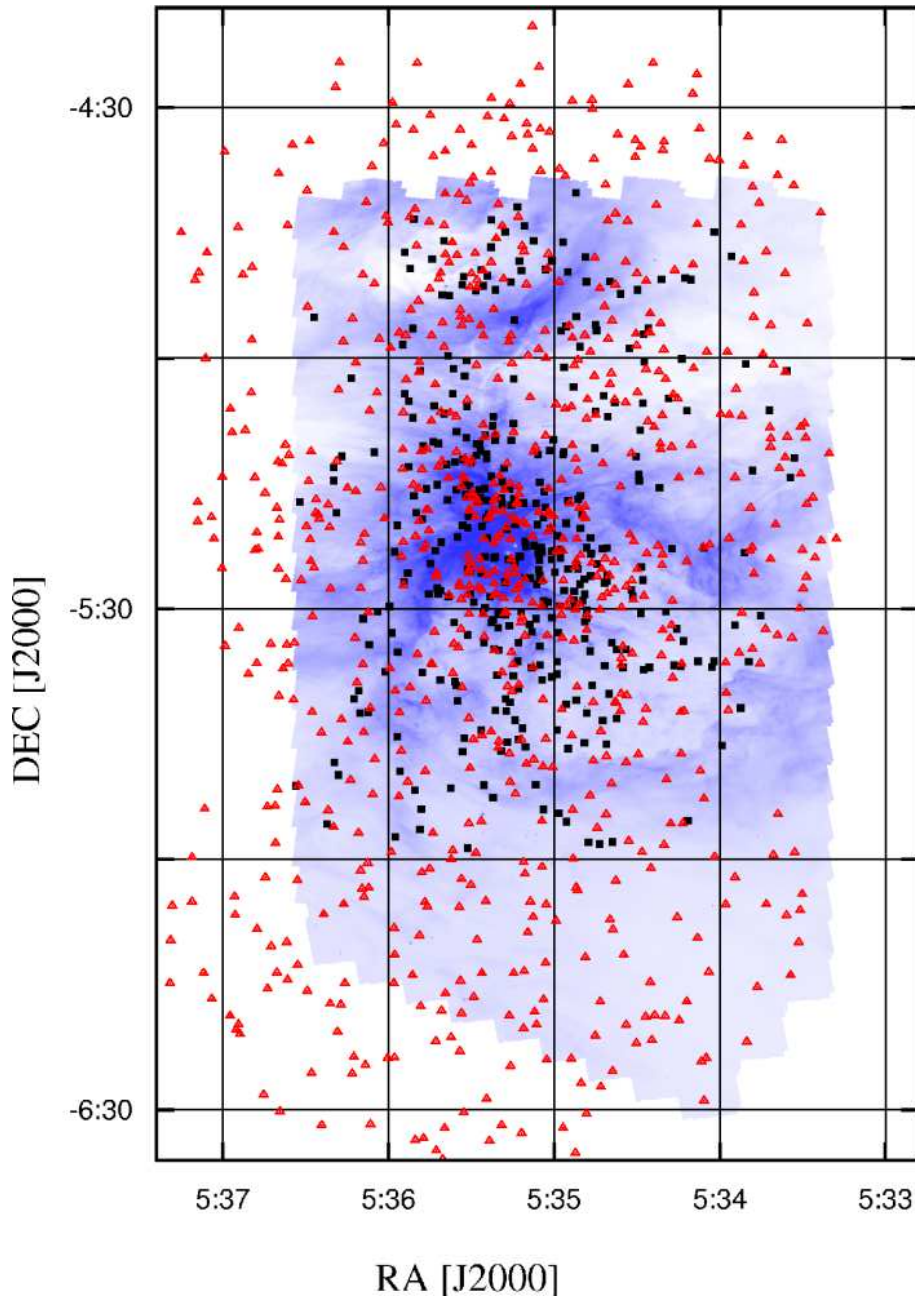


Fig. 1.— Positions of our targets overplotted a IRAC $8\mu\text{m}$ mosaic image of Orion Nebula. The open triangles are stars selected using a 2MASS color-magnitude diagram of the region, the filled squares are targets from Spitzer/IRAC photometry. See text for details. (The triangle symbols were brightened over the central region of ONC, in order to increase contrast against the gray-scaled gas.)

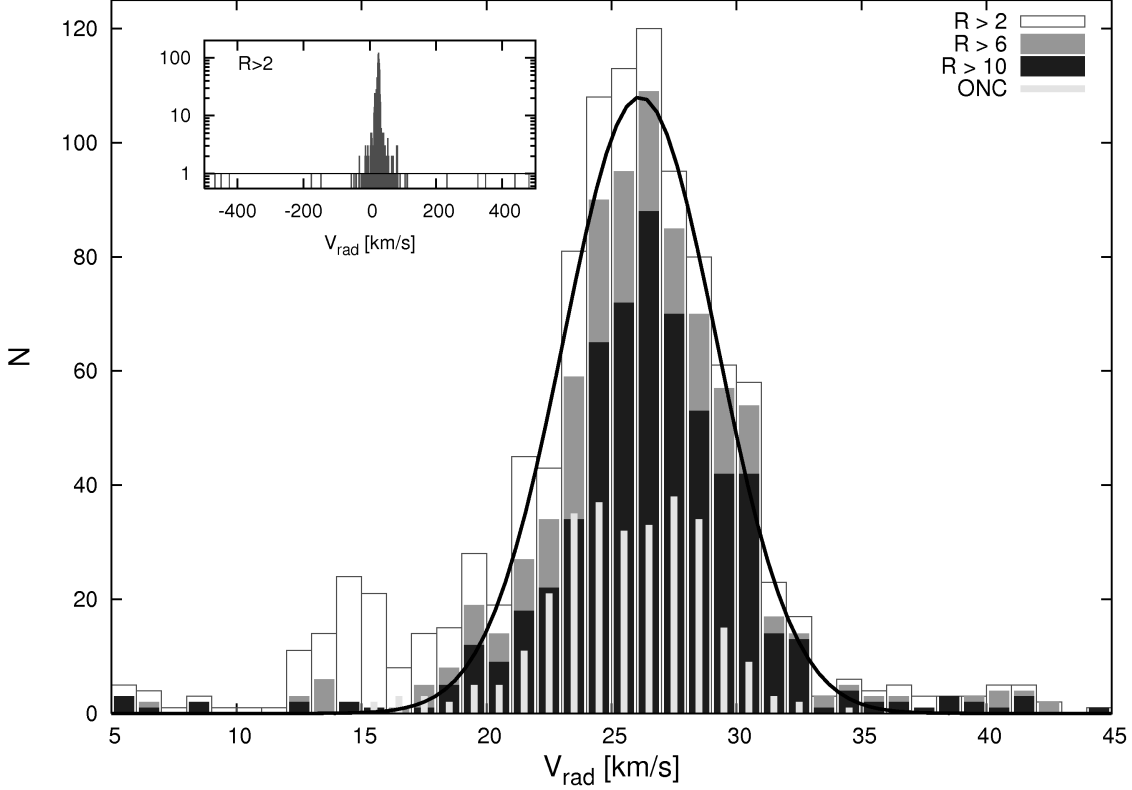


Fig. 2.— Histogram of measured heliocentric radial velocities, displayed for four selections of stars. If the faintest spectra are included, which also yield low S/N ratio (R value) in the cross correlation, a false peak appears in the distribution at the heliocentric correction velocity ($V_{rad} = 14 \text{ km s}^{-1}$). Therefore in the later analysis we only used $R > 4$ spectra, which we found not to be influenced by scattered moonlight. For the main peak the shape is independent of the R value, and can be fitted with a $\sigma = 3.1 \text{ km s}^{-1}$ Gaussian, however there are one relevant departure from the fit at $V_{rad} = 19 \text{ km s}^{-1}$. Distribution of stars within $15'$ of Trapezium are displayed with narrower, light-gray shaded impulses, to show how the distribution of ONC stars compare to the entire region. Note the more flattened peak, but also the agreement in the mean velocity and dispersion. The insert shows the entire 1000 km s^{-1} wide velocity range explored in the cross correlation, and even including the lowest R value spectra ($R > 2$) the global peak around $V_{rad} = 26 \text{ km s}^{-1}$ is very well defined, with only a very few outliers (these are usually faint, noisy spectra).

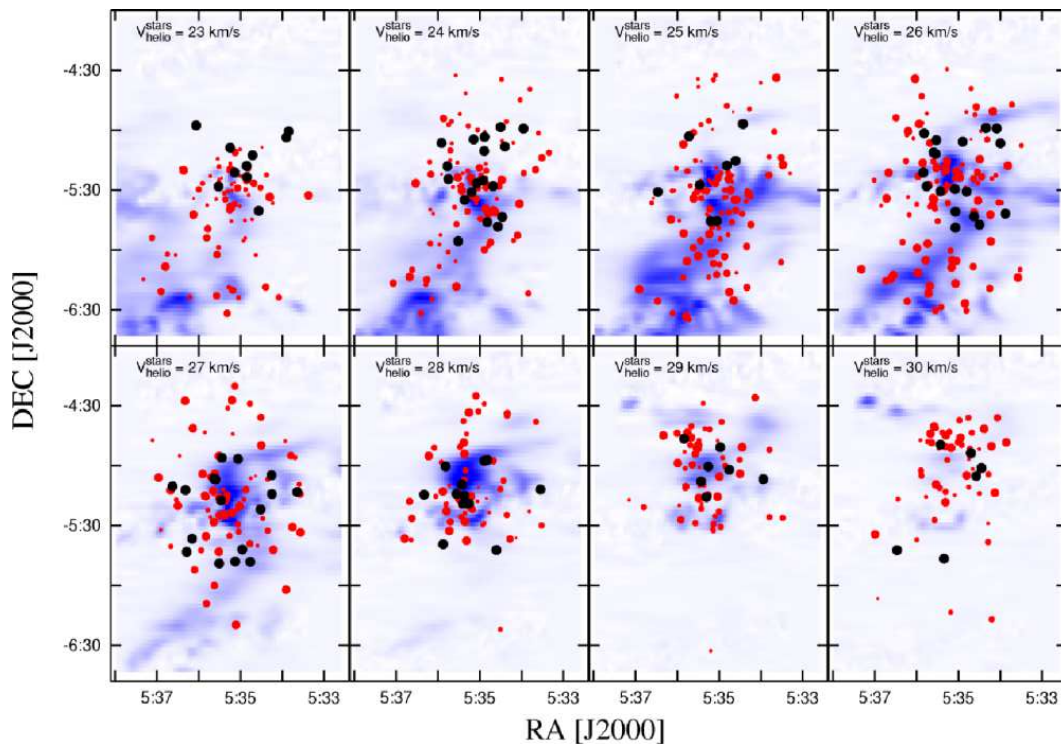


Fig. 3.— Velocity channel maps of the ONC region. The dots represent stars with one (red) or more (black) RV measurements, while blue is the molecular gas observed in ^{13}CO , both displayed in 1 km s^{-1} channels. LSR velocities of the gas is converted to heliocentric ($V_{helio} = V_{LSR} + 17.5$). The size of the dots correspond to the R value, larger dot means more accurate velocity. The north-south velocity gradient is obvious and the correlation between the spatial and density distribution of stars and molecular gas is very significant. This suggests that the stars are still co-moving with the gas clouds in which they formed.

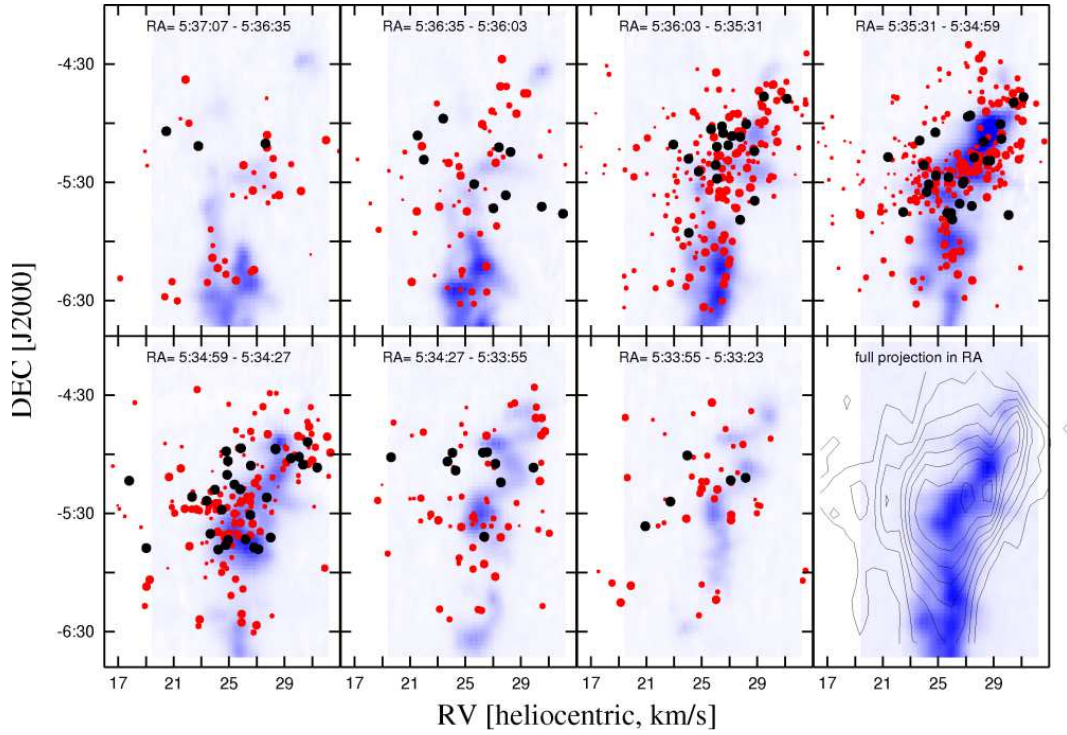


Fig. 4.— Channel maps of the ONC region, in right ascension. Symbols are the same as for Fig. 3. The approximately 30 second wide RA ranges are noted in each channel. The correlation between the gaseous and stellar component is most prominent in the upper right corner, in the channel containing the Trapezium. On the lower right panel a full projection is shown with stellar density contours overlotted the gas distribution.

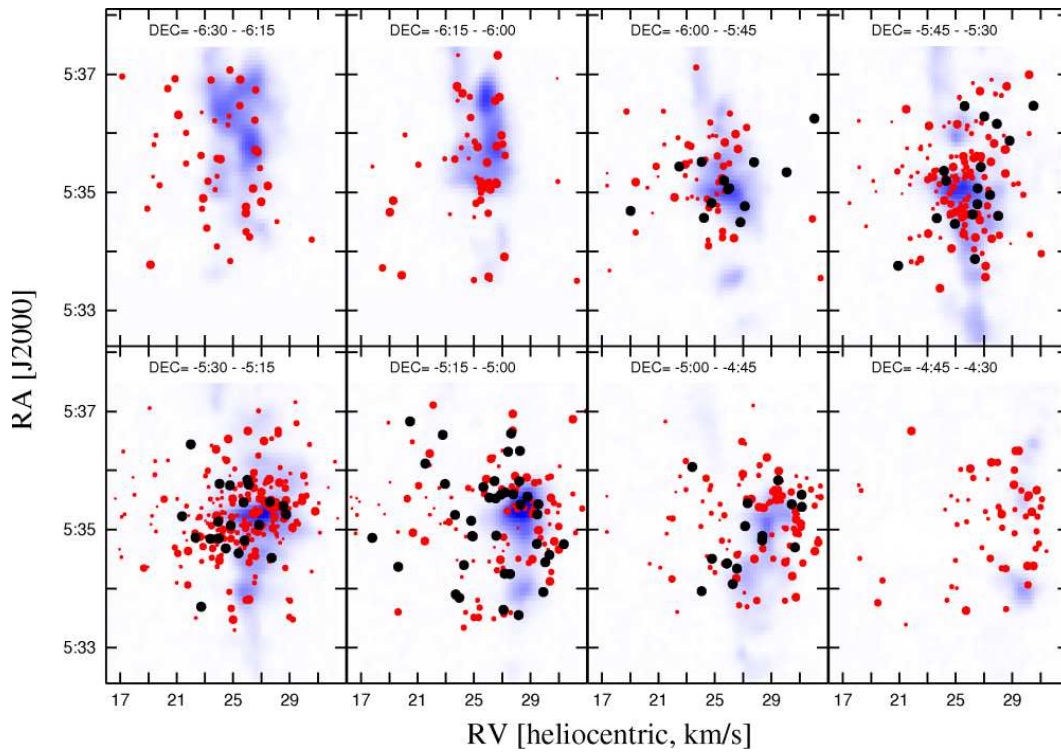


Fig. 5.— Channel maps of the ONC region, in declination. Symbols are the same as for Fig. 3. The 15 arcminute wide DEC ranges are noted in each channel.

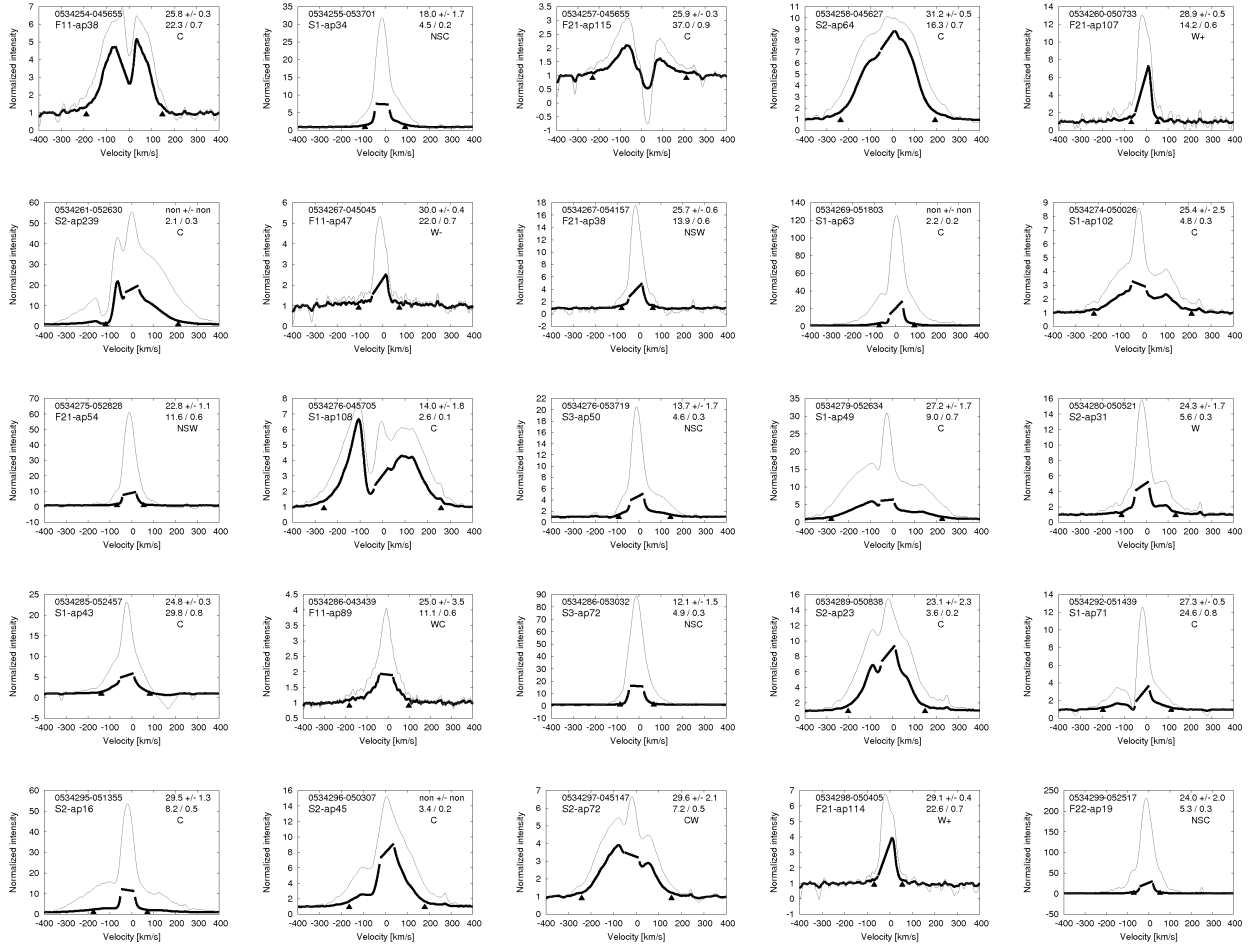


Fig. 6.— Examples of $H\alpha$ profiles for stars with detected emission. Wavelength is converted to velocity with the zero-point being the RV of the star. (In case of very low R values the zero-point is set to $RV=0 \text{ km s}^{-1}$.) 2MASS and internal identification numbers are given in the upper left corner for each stamp, while RV and its error, the R and S values, and note on the $H\alpha$ profile are shown in the upper right (see Table 2 and 3). The thick solid line is the observed spectrum with linear scaling and with the supposed nebular component cut off and replaced by a linear segment. The span of the y axis was scaled to accommodate the peak of the original, unmodified profile, so one can read the relative strength respect to continuum even the peak was found to purely nebular and therefore was cut off. For the original profile, and to emphasize the sometimes barely visible wings, we also show as thin solid line a log scaled version of the observed, unmodified profile. It is scaled to match in peak the original, linear scaled peak height (so the scale does not apply to this). Solid triangles mark the 10% full width for the nebular-line corrected spectrum. [See the electronic edition of the Journal for all observed $H\alpha$ profiles – or contact the authors]

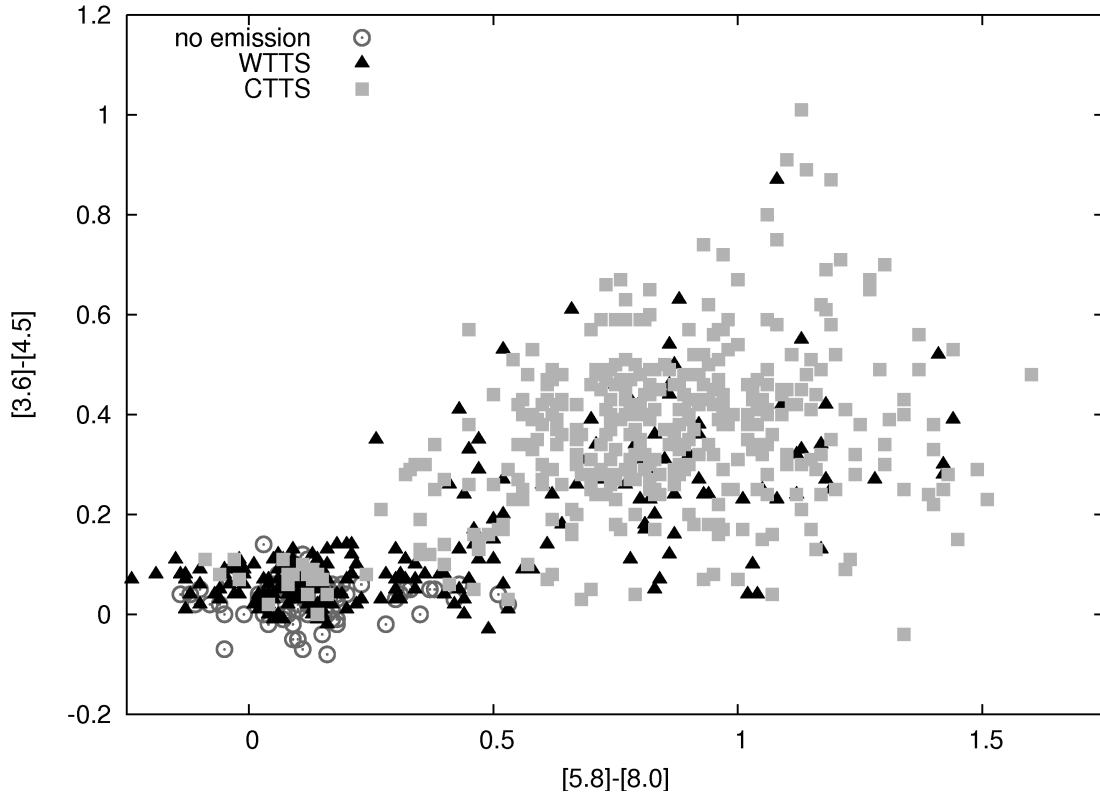


Fig. 7.— IRAC color-color diagram of stars with measured RV. Stars with signs of accretion (wide $H\alpha$ emission, CTTSs) detected in the spectra must have a disk, and accordingly they do exhibit infrared excess (filled squares), occupying the approximate domain of Class II objects (Allen et al. 2004). Among stars showing only weak $H\alpha$ emission (filled triangles) some still exhibit infrared excess, meaning the disk is yet presented but accretion has already stopped. Most of the WTTS stars, however, have no signs of disks and scatter around (0, 0). These Class III objects, exhibiting no intrinsic infrared excess, share the area of the graph with field stars and older cluster members showing no signs of $H\alpha$ emission (open circles).

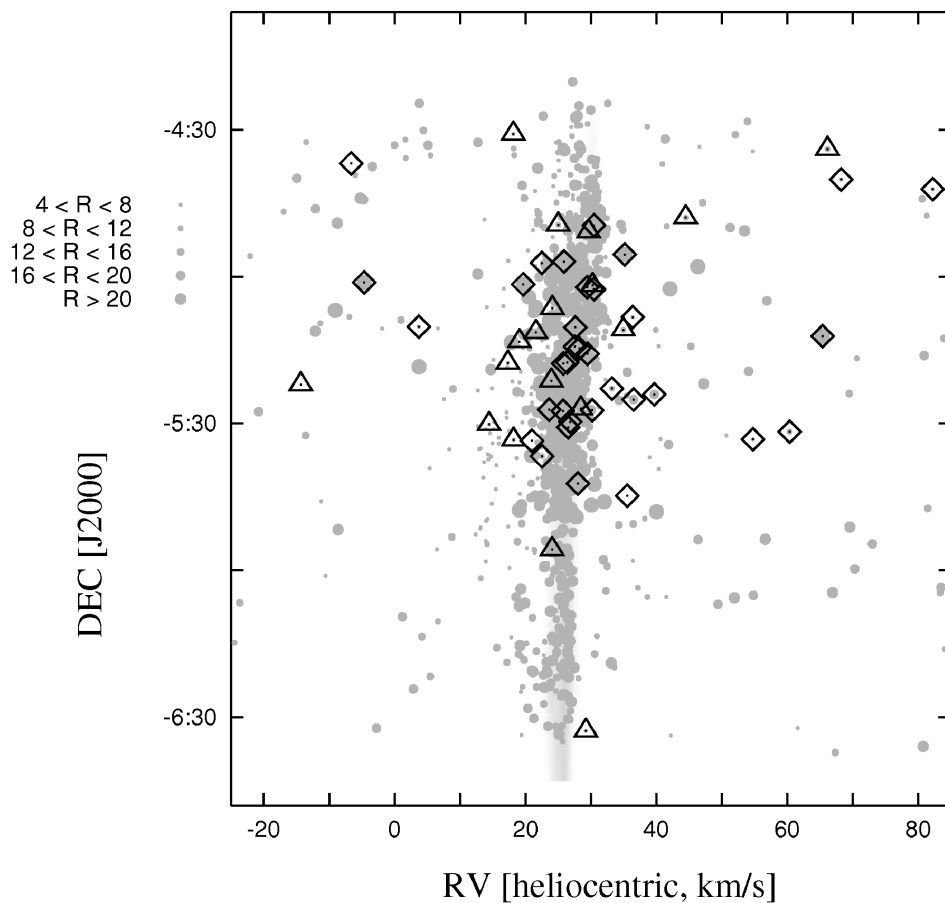


Fig. 8.— Binary stars displayed on a spatial–velocity plot of the ONC region (full projection along RA). The molecular gas is mostly buried by the crowded stellar symbols (gray circles; size is correlated to R value like on Fig. 3). Binaries, identified by clear double peaks in the cross-correlation function or by two different RV measured at two epochs, are shown as open diamonds. (In case of more than one RV value the star is displayed according to the average of the velocities.) Possible binaries, exhibiting asymmetric or side-lobed cross-correlation function, are displayed as open triangles.

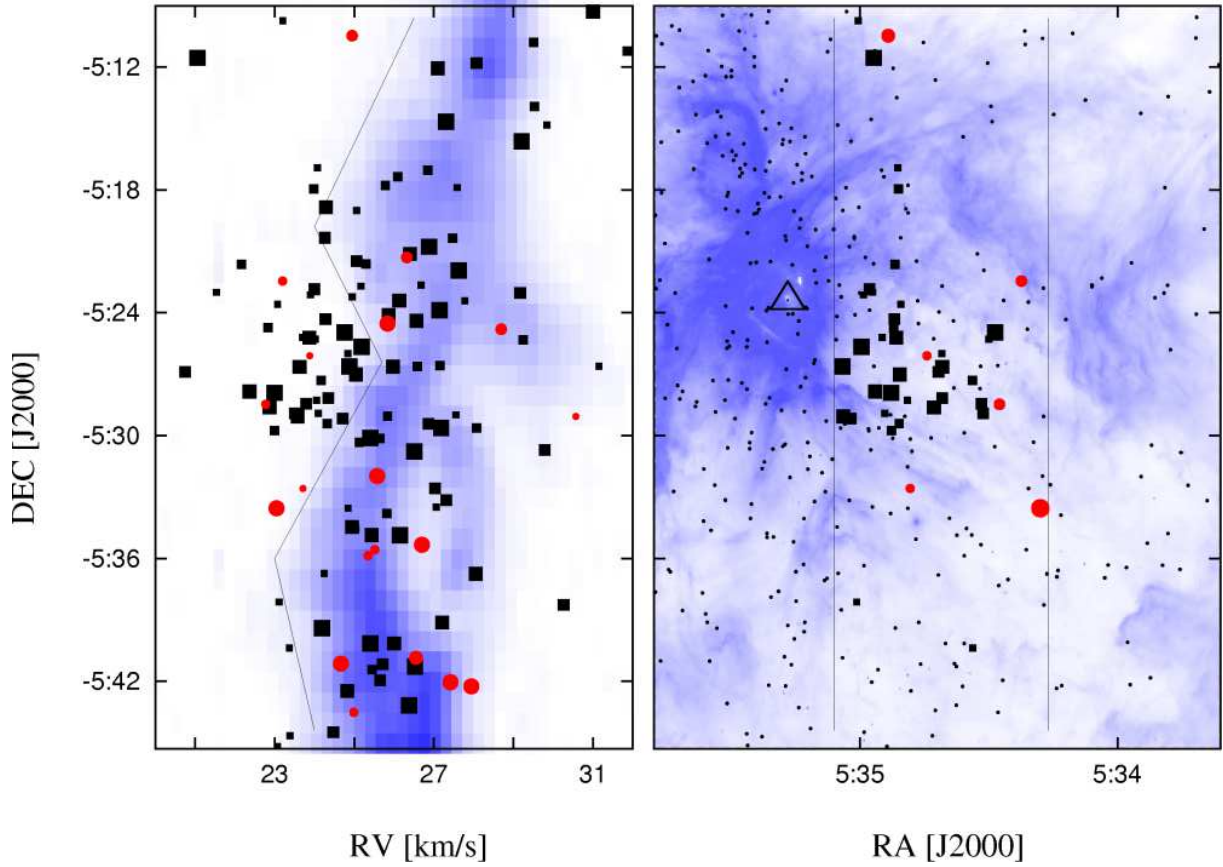


Fig. 9.— In the left panel, we show a zoomed-in velocity–declination channel map similar to the bottom left panel of Fig. 4. A group of stars in the range $-5^d 20^m > DEC > -5^d 30^m$ is slightly but clearly offset from the molecular gas by about $1\text{--}2 \text{ km s}^{-1}$. Most of these stars also show infrared excess (filled squares); only a few do not (open circles), and so are clearly members. We defined a velocity envelope for the ^{13}CO emission (thin curve), and plot the positions of the stars blueward of this envelope in the right panel. These “off-cloud” stars tend to lie in a relatively evacuated region west–south-west of Trapezium (noted as an open triangle), as indicated by the low dust emission seen in the $8\mu\text{m}$ IRAC map (shaded area). All other stars with measured velocities and $R > 4$ are shown as black dots, and two vertical lines represent the RA limits of the channel map on the left. The morphology of the region suggests that molecular gas has recently been evacuated by outflows from the Trapezium region (see text).

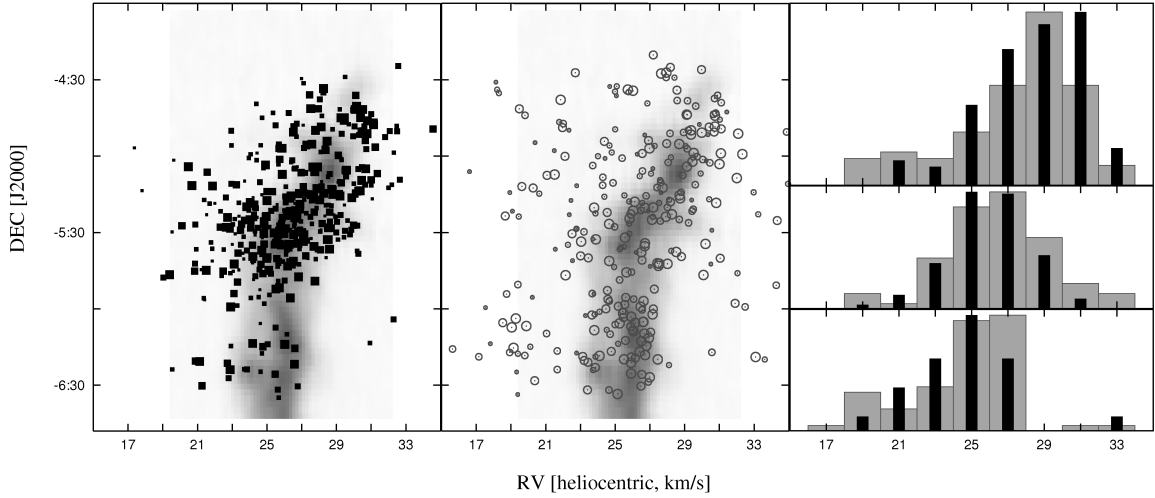


Fig. 10.— Velocity–spatial plot, full projection in RA, of stars with (filled squares, left panel) and without (open circles, middle panel) infrared excess. On the right, we show histograms for three declination bands, which are indicated by the locations of the histograms. Note, that for the northern section ($DEC > -5.2$ deg) the mean velocity of the gas is redshifted, as it is seen in the displaced peak of the distribution as well. The middle ($-5.2 > DEC > -6.0$) and southern ($DEC < -6.0$) sections have similar mean velocities, although there is a strong RV gradient in the mid-declination range. On these histograms the gray shaded columns represent the distribution of the non-excess stars (middle panel), the black bars represent the excess stars (left panel). Note the group of stars around $DEC = -6^d 15^m$ and $RV = 19$ km s^{-1} , which is only apparent on the middle panel (non-excess stars) and could be an older foreground population. This group is responsible for the small local peak at 19 km s^{-1} in the RV histogram of Fig. 2. Also note that at $DEC < -6$ there are less IR excess sources on cloud, which is a selection effect (see text for details).

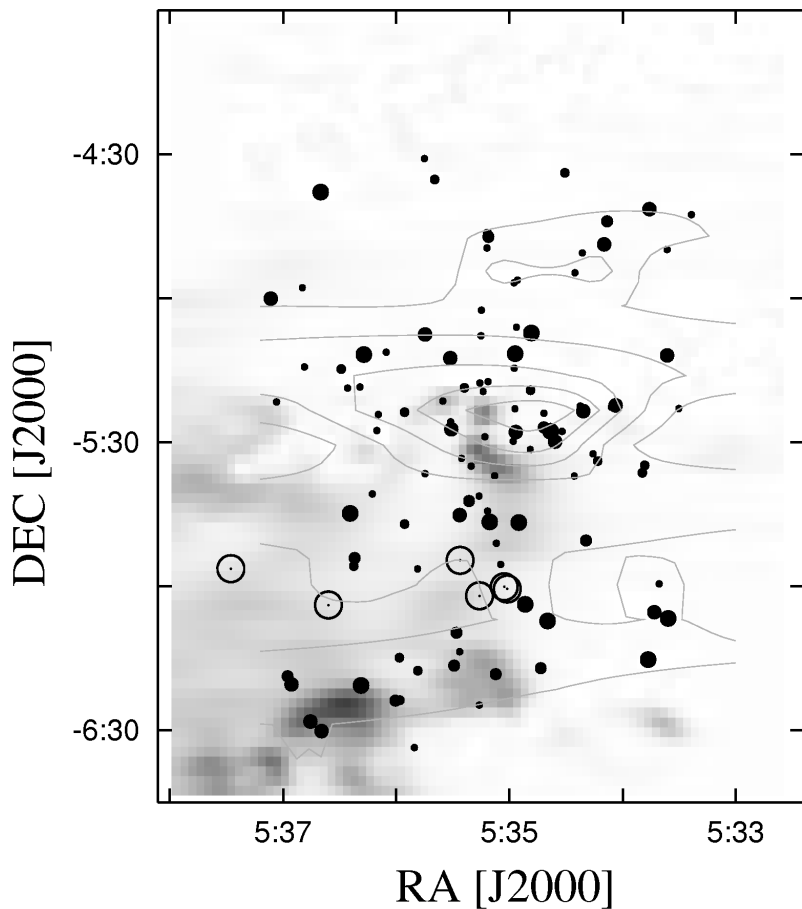


Fig. 11.— Spatial distribution of foreground stars (filled circles), with significantly blue-shifted velocities respect to the molecular cloud (shaded areas). The stars are displayed between $16 < RV < 22 \text{ km s}^{-1}$, and since there is no gas at this heliocentric velocity range, we plot the most blueshifted RA-DEC channel of the gas at $RV = 23 \text{ km s}^{-1}$. Contours of stellar density are also plotted (with levels of 1 star per 0.2×0.2 degree area) Open circles note the OB stars around $DEC \simeq -6^\circ$ (HD 37303, 37209, 37043, 37025, 36960 and 36959).

Table 1. Summary of spectroscopic observations

Date	ID	field center	exposures	binning mode	number of targets
2004 Dec 01	F11	$5^h 35^m 19^s - 04^\circ 49' 27''$	3×20 min	1×1	224
2004 Dec 01	F21	$5^h 35^m 13^s - 05^\circ 21' 14''$	3×20 min	1×1	210
2004 Dec 01	F22	$5^h 35^m 13^s - 05^\circ 21' 14''$	3×20 min	1×1	219
2004 Dec 01	F31	$5^h 35^m 26^s - 06^\circ 07' 30''$	3×20 min	1×1	213
2005 Nov 15	S3	$5^h 35^m 13^s - 05^\circ 33' 10''$	3×15 min	2×2	161
2005 Nov 15	S2	$5^h 35^m 11^s - 05^\circ 07' 28''$	3×15 min	2×2	154
2005 Nov 15	S1	$5^h 35^m 21^s - 05^\circ 18' 50''$	3×15 min	2×2	170

Table 2. Members

2MASS_id	ID	J	(J - H)	(H - K)	[3.6 - 4.5]	[5.8 - 8.0]	V_{rad}	ΔV_{rad}	R	S	EW_c	$FW_{10\%}$	H α	CCF	NOB
0533179-052138	F22-ap25	13.18	0.87	0.24	0.00	0.00	25.09	6.38	4.4	0.39	11.2	239	W	w	1
0533204-051123	F21-ap89	12.73	1.07	0.29	0.00	0.00	24.28	0.53	13.6	0.58	5.2	169	W	c	1
0533225-053240	F22-ap20	13.02	0.98	0.23	0.00	0.00	23.89	0.35	22.4	0.71	5.3	134	W	c	1
0533233-052153	F22-ap27	12.90	0.87	0.24	0.00	0.00	47.20	0.35	23.4	0.74	0.9	179	W	c	1
0533234-044234	F11-ap62	13.38	0.94	0.34	0.00	0.00	21.48	4.60	5.0	0.23	3.7	152	W	w,l	1
0533256-052354	F21-ap61	13.32	0.95	0.21	0.02	-	69.48	0.49	15.1	0.64	2.4	178	W	c	1
0533263-051640	F22-ap37	13.34	1.25	0.33	0.00	0.44	70.65	0.64	10.7	0.54	5.2	189	NSW	c	1
0533285-051726	F22-ap40	11.92	1.12	0.34	0.04	0.79	25.01	0.32	28.7	0.85	23.1	390	C	c	1
0533287-052610	F21-ap69	13.23	1.08	0.29	0.02	0.12	29.23	0.82	12.1	0.53	6.6	116	NSW	c	1
0533293-050749	F22-ap49	13.29	1.20	0.32	0.03	0.00	26.42	2.32	10.1	0.62	4.0	184	W-	c	1
0533301-052257	F22-ap30	13.03	0.79	0.21	0.02	0.00	22.36	2.34	6.8	0.48	2.3	153	W	c	1
0533302-060409	F31-ap51	12.26	0.89	0.22	0.00	0.14	32.28	3.01	14.8	0.81	7.0	448	C	w	1
0533307-051352	F21-ap86	13.16	0.89	0.21	0.24	0.44	25.00	0.58	18.5	0.70	4.2	146	NSW	c	1
0533307-051351	S2-ap26	13.16	0.89	0.21	0.24	0.44	25.32	0.63	16.9	0.72	2.0	164	W-	c	1
0533307-050813	F21-ap94	13.02	1.11	0.31	0.01	0.02	-6.91	0.73	10.4	0.60	0.0	0	W	c	1
0533310-060605	F31-ap57	13.07	0.91	0.21	0.05	0.13	25.00	0.75	15.9	0.71	2.4	142	W+	c	1
0533312-052957	F22-ap13	13.45	1.01	0.32	0.23	1.51	28.98	0.44	14.9	0.57	33.0	229	C	c	1
0533314-060954	F31-ap52	12.75	1.08	0.36	0.34	0.94	26.16	0.88	11.2	0.51	52.1	293	C	c	1
0533329-055909	F31-ap66	12.10	0.75	0.23	0.01	0.14	32.48	0.57	14.1	0.67	0.0	0	AE	c	1
0533330-051155	S1-ap75	12.57	1.22	0.42	0.25	0.98	28.16	0.39	14.7	0.62	8.5	335	C	c	2
0533339-053326	F22-ap14	12.21	1.25	0.40	0.26	0.67	27.11	0.40	21.2	0.76	4.9	181	W	c	1
0533343-061352	F31-ap48	12.72	0.94	0.20	0.00	0.00	26.03	0.35	24.2	0.79	3.6	383	C	c	1
0533344-051417	S1-ap78	12.48	1.12	0.38	0.47	1.04	27.12	0.60	17.8	0.72	4.1	308	CW	c	1
0533357-050923	F21-ap92	12.50	1.09	0.28	0.06	0.08	27.59	6.19	8.1	0.51	4.9	354	CW	w	1
0533358-050132	S2-ap44	11.72	1.34	0.51	0.43	0.93	24.41	0.81	10.7	0.58	39.1	473	C	c	1

Note. — Hectochelle targets in ONC found to be members based on measured RV value or by detected H α emission. The criteria of being RV member is to have at least one velocity measurement within 4σ of the cluster mean velocity: $13.7 \text{ km s}^{-1} < V_{helio} < 38.5 \text{ km s}^{-1}$. RV members listed only with $R > 2$, while stars with H α emission are included regardless of R value, but with no velocity displayed. – for the full table see the electronic version of the Jurnal or contact the authors)

2MASS id — 2MASS identification number (truncated RA and DEC coordiantes as: HHMMSSS+DDMMSS); **ID** — internal identification number, specifying the field (see Table 1) and aperture of observation. The letter *F* means the first run, and therefore 2MASS based selection, the letter *S* notes IRAC based selction and observation taken during the 2nd run; **J** — 2MASS J magnitude; **(J-H)** — 2MASS (*J-H*) color index; **(H-K)** — 2MASS (*H-K*) color index; 3.6–4.5 — IRAC short wavelength color index; 5.8–8.0 — IRAC long wavelength color index; V_{rad} — measured heliocentric radial velocity, in km s $^{-1}$; V_{rad} — *xcsao* error estimate for V_{rad} , in km s $^{-1}$; **R**

— R value of cross correlation (see text for details); **S** — height of the CCF peak; EW_c — absolute value of equivalent width, measured on the corrected $H\alpha$ profile (see text for details); $FW_{10\%}$ — full width of $H\alpha$ profile at 10% level of the corrected maximum (see text for details);

H α — notes on the $H\alpha$ emission profile. See text for more details on the CTTS/WTTS classification: **C** – CTTS; **W** – WTTS; **CW** – rather CTTS, but could be WTTS; **WC** – rather WTTS, but could be CTTS; **W+** – asymmetry in line profile/wing: likely WTTS; **W-** – asymmetry in wings, but wings at low intensity: could be WTTS; **D** – resolved or unresolved double gaussian profile, no excess H-alpha emission (likely non-TTS); **CD** – resolved or unresolved double gaussian profile, likely CTTS; **WD** – resolved or unresolved double gaussian profile, likely WTTS; **R** – obviously shifted H-alpha absorption : high RV stars; **X** – very wide H-alpha absorption with nebular emissions; **CX** – CTTS, with strange emission profiles; **AE** – stellar absorption and nebular emission together; **NS** – very strong nebular component component, no wings, no asymmetry; **NSC** – like NS, but if intensity logscaled wide wings/asymmetry is visible and suggest CTTS emission signature under the strong nebular component; **NSW** – like NS, but if intensity logscaled narrow wings/asymmetry is visible and suggest WTTS emission signature under the strong nebular component; **SAT** – saturated, or neighbour saturated;

CCF — notes on the cross-correlation function: **w** – wide peak, results large errors in RV; **l** – very low peak, but still sticks out from surrounding; **u** – almost undefined, very low/wide peak; **n** – very noisy (several local peaks, almost as high as the one picked); **s** – side lobed, could be a spectroscopic binary; **d** – double peak, spectroscopic binary; **dv** – RV measured more than once, found different velocities, could be binary; **r** – template spectra with highest peak in cross-correlation resulted non-realistic velocity, so the template resulting in highest R value was used instead to determine velocity; **c** – clear, well-isolated peak; **?** – uncertainty in assigning the given note;

NOB — number of observations

Table 3. Non-members

2MASS_id	ID	J	(J - H)	(H - K)	[3.6 - 4.5]	[5.8 - 8.0]	V_{rad}	ΔV_{rad}	R	S	EW_c	$FW_{10\%}$	H α	CCF	NOB
0533283-045549	F11-ap48	13.27	0.89	0.24	0.04	0.03	-22.07	0.94	8.9	0.46	0.0	0	AE	c	1
0533289-050930	F22-ap46	12.16	1.04	0.30	0.05	0.37	106.39	0.53	13.2	0.61	0.0	0	R	c	1
0533298-052735	F21-ap66	13.31	0.88	0.25	0.02	0.53	-20.75	0.47	19.2	0.74	0.0	0	AE	c	1
0533333-043918	F11-ap67	12.89	0.91	0.27	0.00	0.00	-6.00	0.62	11.5	0.49	0.0	0	AE	c	1
0533363-050140	F11-ap35	13.29	0.80	0.21	0.00	0.00	-	-	2.1	0.17	0.0	0	AE	w,l	1
0533390-055434	F31-ap72	12.59	1.62	0.40	-0.02	0.04	73.01	0.38	19.7	0.70	0.0	0	AE	c	1
0533415-050934	F22-ap50	13.19	0.96	0.24	0.08	-0.03	-11.32	0.81	9.8	0.58	0.0	0	AE	c	1
0533445-045930	F11-ap31	12.62	1.05	0.23	-0.07	0.11	12.70	0.34	20.5	0.72	0.0	0	AE	c	1
0533497-043329	F11-ap73	13.47	0.98	0.25	0.00	0.00	46.59	0.89	7.4	0.34	0.0	0	AE	c	1
0533514-043655	F11-ap78	13.37	1.25	0.34	0.00	0.00	-6.63	10.17	2.9	0.22	0.0	0	AE	d,l	1
0533520-050655	F21-ap93	12.76	0.92	0.27	0.02	-0.06	-9.05	0.38	12.7	0.56	0.0	0	N	c	2
0533524-044400	F11-ap64	12.12	1.20	0.30	-0.01	0.17	-5.25	0.34	21.6	0.72	0.0	0	AE	c	1
0533570-054210	F22-ap235	12.08	1.66	0.44	-0.08	0.16	112.78	0.46	15.2	0.68	0.0	0	R	c	1
0533579-060524	F31-ap53	13.10	0.80	0.24	0.06	0.04	38.64	0.76	10.1	0.60	0.0	0	AE	c	1
0534018-055941	F31-ap69	13.17	1.24	0.32	0.00	0.12	70.32	0.37	19.2	0.71	0.0	0	AE	c	1
0534040-061329	F31-ap44	12.70	0.80	0.20	0.01	0.17	4.17	0.57	15.1	0.75	0.0	0	AE	c	1
0534057-062851	F31-ap22	11.77	1.31	0.38	0.00	0.00	113.63	0.41	18.0	0.68	0.0	0	R	c	1
0534071-054925	F31-ap82	13.17	1.12	0.35	0.02	-0.11	38.22	0.75	10.3	0.49	0.0	0	AE	c	1
0534073-043231	F11-ap82	12.86	0.91	0.29	0.00	0.00	-13.51	0.74	10.3	0.49	0.0	0	AE	c	1
0534080-060924	F31-ap41	13.46	1.03	0.29	0.01	0.10	1.20	0.45	18.9	0.74	0.0	0	AE	c	1
0534095-050111	F11-ap21	13.18	1.01	0.25	0.04	-0.14	-4.65	0.60	10.3	0.57	0.0	0	AE	c,dv	2
0534098-042819	F11-ap87	12.08	0.69	0.21	0.00	0.00	53.92	0.60	13.4	0.67	0.0	0	AE	c	1
0534104-051020	F22-ap54	12.97	0.95	0.31	0.06	0.43	-40.46	0.91	8.4	0.53	0.0	0	R	c	1

Note. — Hectochelle targets in ONC found to be non-members based on measured RV value or lack of detected H α emission. Stars are listed regardless of R value, but no velocity is displayed in case of very low R or undefined CCF. — For the full table see the electronic version of the Journal or contact the authors.

2MASS id — 2MASS identification number (truncated RA and DEC coordinates as: HHMMSS+DDMMSS); **ID** — internal identification number, specifying the field (see Table 1) and aperture of observation. The letter *F* means the first run, and therefore 2MASS based selection, the letter *S* notes IRAC based selection and observation taken during the 2nd run; **J** — 2MASS J magnitude; **(J-H)** — 2MASS (*J-H*) color index; **(H-K)** — 2MASS (*H-K*) color index; **3.6-4.5** — IRAC short wavelength color index; **5.8-8.0** — IRAC long wavelength color index; V_{rad} — measured heliocentric radial velocity, in km s⁻¹; ΔV_{rad} — *xcsao* error estimate for V_{rad} , in km s⁻¹; **R** — R value of cross correlation (see text for details); **S** — height of the CCF peak; EW_c — absolute value of equivalent width, measured on the corrected H α profile (see text for details); $FW_{10\%}$ — full width of H α profile at 10% level of the corrected maximum (see text for details);

H α — notes on the H α emission profile: **D** — resolved or unresolved double gaussian profile, no excess H-alpha emission (likely non-TTS); **R** — obviously shifted

H-alpha absorption : high RV stars; **X** — very wide H-alpha absorption with nebular emissions; **AE** — stellar absorption and nebular emission together; **NS** — very strong nebular component component, no wings, no asymmetry; **CCF** — notes on the cross-correlation function: **w** – wide peak, results large errors in RV; **l** – very low peak, but still sticks out from surrounding; **u** – almost undefined, very low/wide peak; **n** – very noisy (several local peaks, almost as high as the one picked); **s** – side lobed, could be a spectroscopic binary; **d** – double peak, spectroscopic binary; **dv** – RV measured more than once, found different velocities, could be binary; **r** – template spectra with highest peak in cross-correlation resulted non-realistic velocity, so the template resulting in highest R value was used instead to determine velocity; **c** – clear, well-isolated peak; **?** – uncertainty in assigning the given note;
NOB — number of observations